International Journal on Magnetic Particle Imaging
Vol 3, No 1, Article ID 1703014, 7 Pages

Infinite Science Publishing

Research Article

Influence of the Receive Channel Number on the Spatial Resolution in Magnetic Particle Imaging

Patryk Szwargulski[a,b,*], Tobias Knopp[a,b]

[a]Section for Biomedical Imaging, University Medical Center Hamburg-Eppendorf, Hamburg, Germany
[b]Institute for Biomedical Imaging, Hamburg University of Technology, Hamburg, Germany
[*]Corresponding author, email: p.szwargulski@uke.de

Received 28 November 2016; Accepted 1 March 2017; Published online 23 March 2017

Abstract

Magnetic Particle Imaging (MPI) is a fast and highly sensitive tomographic imaging modality. When applying 3D Lissajous imaging sequences, the region of interest is rapidly sampled by moving a field-free point along a predefined trajectory. Since the field excitation is done using three orthogonal excitation coils, usually also the magnetization response is measured with three independent and orthogonal receive coils. In this work the influence of selecting a subset of receive channels during reconstruction on the resulting image quality is analyzed. It is shown that using a single receive channel a slight loss of spatial resolution in the order of 12 % to 22 % in the direction perpendicular to the receiving direction can be observed while in direction of the receive coil the resolution is preserved and partially even improved. Since the construction of decoupled 3D receive coil units is a major engineering effort, the findings can be used to simplify the construction of 3D Lissajous type scanners.

I. Introduction

Magnetic Particle Imaging (MPI) is a multidimensional tomographic imaging modality featuring high temporal and spatial resolution in combination with a high sensitivity for the detection of superparamagnetic iron-oxide nanoparticles (SPIOs) that serve as contrast agents in MPI. Since the invention of MPI in 2001 many different scanner types have been developed [1–7]. All scanners have in common that they excite the nanoparticles with a sinusoidal magnetic field and they differ in either the selection field or the sampling trajectory. The selection field responsible for spatial encoding in MPI can either be a field-free point (FFP) [2] or a field-free line (FFL) gradient field [8, 9]. The trajectory is usually chosen to be Cartesian, Lissajous, or Radial [10].

Cartesian trajectories have the advantage that they require a single excitation and receive channel since the particle magnetization and the send/receive channel orientation are perfectly aligned. Lissajous type scanners require for each imaging dimension a dedicated excitation channel such that for 3D imaging three orthogonal send coils are required. Since the particle magnetization during a 3D Lissajous sequence will change during excitation, it is common to use three orthogonal pick-up coils to recover the full direction of the magnetization over time. While constructing a 3D receiving unit is feasible [11] it is still an open question if three receive channels for the reconstruction of 3D Lissajous data are actually required. In [12] the 3D MPI system function has been analyzed and it has been shown that the individual receive channels carry highly redundant information. In partic-

10.18416/ijmpi.2017.1703014

ular each spatial pattern of the system function within a certain receive channel will occur similarly in each of the other receive channels at a different frequency.

The purpose of this work is to investigate experimentally using a preclinical 3D MPI scanner how the image quality is effected when using only a single receive channel for the reconstruction of 3D data. In particular we will study the impact of the number of receive channels on the spatial resolution of reconstructed images.

II. Materials and Methods

II.I. Experimental Setup

Experiments are carried out using a preclinical MPI scanner (Bruker Biospin, Germany) having a 118 mm bore diameter allowing to image small animals as for instance mice, rats, and small rabbits. The scanner is equipped with a Maxwell coil pair oriented in z direction (vertical) generating the FFP field with adjustable gradient strength. The gradient strength in z direction is twice the gradient strength in x/y direction leading to an anisotropic spatial resolution, where the higher resolution will be observed along the z direction. In all experiments the gradient strength is set to $G_z = -2G_x = -2G_y = 1.5\,\mathrm{T/m}$.

The FFP is steered along a 3D Lissajous trajectory using three orthogonal drive field coils generating an almost homogeneous magnetic field in the respective direction. The drive field frequencies are hardwired within the scanner and given by $f_x = 2.5\,\mathrm{MHz}/102$, $f_y = 2.5\,\mathrm{MHz}/96$, and $f_z = 2.5\,\mathrm{MHz}/99$. The drive-field amplitudes are set to $A_x = A_y = A_z = 14\,\mathrm{mT}$ leading to a field of view (FOV) covered by the Lissajous trajectory of $37.33 \times 37.33 \times 18.66\,\mathrm{mm}^3$.

The system matrix required for reconstruction is measured on a grid of size $30 \times 30 \times 35$ covering a region of interest of $60 \times 60 \times 35\,\mathrm{mm}^3$. The matrix is measured using a delta sample of size $2 \times 2 \times 1\,\mathrm{mm}^3$ that is filled with undiluted (500 mmol(Fe)/L) ferucarbotran (Resovist, Irom Pharmaceuticals, Tokio, Japan). The system matrix is acquired with an averaging factor of 30.

The spatial resolution of the system is determined and evaluated in two steps. First, a dot phantom of the same size as for system calibration but with a reduced particle concentration of 125 mmol(Fe)/L is used. The phantom is shown in Fig. 1 (left) where the delta sample is mounted on the calibration rod. The spatial resolution is then determined by analyzing the full-width at half maximum (FWHM) of the reconstructed dot. In order to evaluate the determined resolution a dedicated resolution phantom is used that consists of five glass capillaries with an inner diameter of 1.3 mm and an outer diameter of 1.7 mm. The capillaries are arranged in a way that one capillary is located in the center and in the other capillaries are arranged in x and y directions with a distance of 4.3 mm and 7.3 mm. Including the thickness of the capillaries the tracer to tracer distance is 4.7 mm and 7.7 mm. A patch panel with defined distances is used for mounting the glass capillaries. The setup of the resolution phantom is shown in Fig. 1. Each of the glass capillaries is filled 20 mm high with 125 mmol(Fe)/L ferucarbotran. All measurements are performed with an averaging factor of 1000 leading to an acquisition time of 21.54 s.

Figure 1: Picture of a delta sample mounted on the calibration rod (left) and the used glass capillaries filled with ferucarbotran (middle) that are mounted on a patch panel to setup the resolution phantom (right). The distances between the capillaries in both directions are 4.3 mm and 7.3 mm.

II.II. Frequency Selection

For each receive channel $l = x, y, z$ the relation between the particle concentration $\boldsymbol{c}$ and the measured voltage signal in frequency space $\boldsymbol{u}_l$ can be formulated as a linear system of equations

$$\boldsymbol{S}_l \boldsymbol{c} = \boldsymbol{u}_l. \tag{1}$$

Since the system matrix for each channel is determined in a measurement procedure, the matrices are affected by noise and will contain rows carrying no MPI signal. These rows are usually removed prior to reconstruction by applying a threshold filter [13]. Within this work we use only those matrix rows that have a signal to noise ratio (SNR) greater than 2.5. The SNR is calculated by relating the signal to a reference scan that is measured with an empty scanner bore [1]. The reduced imaging equations can be formulated as

$$\boldsymbol{S}_l^{\mathrm{red}} \boldsymbol{c} = \boldsymbol{u}_l^{\mathrm{red}}. \tag{2}$$

In order to take all three receive channels during reconstruction into account one usually combines the three individual linear system of equations (2) by stacking the system matrices and measurement vectors leading to

$$\begin{pmatrix} \boldsymbol{S}_x^{\mathrm{red}} \\ \boldsymbol{S}_y^{\mathrm{red}} \\ \boldsymbol{S}_z^{\mathrm{red}} \end{pmatrix} \boldsymbol{c} = \begin{pmatrix} \boldsymbol{u}_x^{\mathrm{red}} \\ \boldsymbol{u}_y^{\mathrm{red}} \\ \boldsymbol{u}_z^{\mathrm{red}} \end{pmatrix}. \tag{3}$$

In order to determine the impact of the number of receive channels on the spatial resolution we will use both Eq. (2) and Eq. (3) for reconstruction and analyze the resulting image data. In addition we will also consider the case where Eq. (3) is adapted to take a combination of two receive channels into account.

10.18416/ijmpi.2017.1703014

Data Redundancy Analysis

In this section we investigate data redundancies across the three channels by studying the structure of the 3D system function. This is based on the system function analysis carried out in [12].

According to this publication, each row of the three matrices $\boldsymbol{S}_l$, $l = x, y, z$ can be approximated by a tensor product of Chebyshev polynomials as

$$\begin{aligned} S^l_{n^l_x,n^l_y,n^l_z}(x,y,z) = \sigma^l_{n^l_x,n^l_y,n^l_z} &\sin\left(n^l_x \arccos\frac{2x}{R_x}\right) \\ &\times \sin\left(n^l_y \arccos\frac{2y}{R_y}\right) \\ &\times \sin\left(n^l_z \arccos\frac{2z}{R_z}\right). \end{aligned} \tag{4}$$

Here, $\sigma^l_{n^l_x,n^l_y,n^l_z}$ is a scalar complex prefactor that differs significantly for different matrix rows and is usually not given in analytical form. The size of the drive field FOV covered by the FFP is given by the factors R_l, $l = x, y, z$. Note that Eq. (4) is given as a continuous function which has to be appropriately sampled to obtain a discrete row of one of the system matrices $\boldsymbol{S}_l$, $l = x, y, z$. The polynomial degrees n^l_x, n^l_y, n^l_z are directly related to the mixing factors m_x, m_y, m_z that on the other hand are directly related to the index k of the considered matrix row. In particular it holds that

$$k = |528m_x + 561m_y + 544m_z|, \tag{5}$$

where the three factors $528 = f_x/\Delta f$, $561 = f_y/\Delta f$, and $544 = f_z/\Delta f$ are derived from the ratios of the excitation frequencies and the spectral resolution Δf [12]. The spectral resolution is defined as the inverse repetition time $\Delta f = 1/T_R$. While the mixing factors are receive channel independent, the channel dependent polynomial degrees are given by

$$n^x_x = |m_x|, \quad n^x_y = |m_y| + 1, \quad n^x_z = |m_z| + 1 \tag{6}$$

$$n^y_x = |m_x| + 1, \quad n^y_y = |m_y|, \quad n^y_z = |m_z| + 1 \tag{7}$$

$$n^z_x = |m_x| + 1, \quad n^z_y = |m_y| + 1, \quad n^z_z = |m_z|. \tag{8}$$

Thus, we can in turn represent a fixed row of one of the receive channels by a corresponding row from another receive channel using

$$\begin{aligned} S^x_{n^x_x,n^x_y,n^x_z}(x,y,z) &= \frac{\sigma^y_{n^y_x-1,n^y_y+1,n^y_z}}{\sigma^x_{n^x_x,n^x_y,n^x_z}} S^y_{n^y_x-1,n^y_y+1,n^y_z}(x,y,z) \\ &= \frac{\sigma^z_{n^z_x-1,n^z_y,n^z_z+1}}{\sigma^x_{n^x_x,n^x_y,n^x_z}} S^z_{n^z_x-1,n^z_y,n^z_z+1}(x,y,z). \end{aligned} \tag{9}$$

The same pattern thus occurs at a shifted matrix row and is weighted by a different prefactor.

In a noise-free setup Eq. (9) would predict that the image quality and in particular the spatial resolution would be independent of the number of receive channels used for reconstruction. However, one important observation that can be derived from Eq. (9) is that the same patterns have a different weighting factor for different receive channels. When assuming a constant noise level this implies that the system matrix rows corresponding to the same polynomial degree have a different SNR. In turn it will happen that certain patterns are above the noise level in only one of the receive channels. When omitting this receive channel during reconstruction, the image quality will be degraded due to the loss of information.

The varying SNR of equivalent system matrix patterns are illustrated in Fig. 2, where beside the SNR also the patterns itself are shown. It is important to note that there is also a global sensitivity difference between the receive channels for the MPI scanner considered in this work. This is due to different FOV distances and shapes of the receive coils leading to different coil sensitivities. For the scanner used in this work, the solenoidal x receive coil has the highest sensitivity.

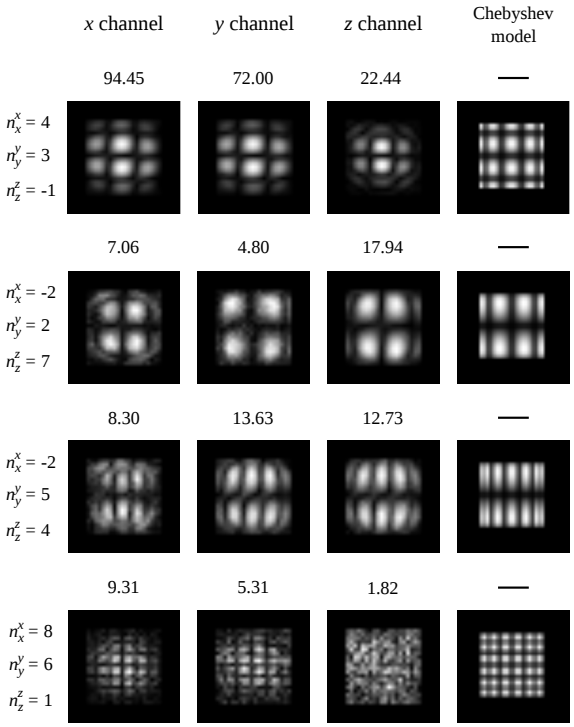

Figure 2: Representation of the redundancy of system matrix rows across the receive channels in comparison with a simulated Chebyshev model. Shown are central slices within the $x\,y$ plane of the 3D system matrix patterns. For each pattern the SNR is given above the shown picture. For each row the channel dependent polynomial degrees (n^x_x, n^y_y, n^z_z) encoding the corresponding spatial pattern are given on the left side. Using Eq. (5) to Eq. (8) for each channel the corresponding frequency component can be calculated.

To get an idea which patterns are present for reconstruction after frequency selection in the different receive

channels, a color coded mask of the frequency selection is shown in Fig. 3. Instead of the frequency index k we plot the mask against the polynomial degrees n_x, n_y, and n_z. From the resulting 3D mask we show the three orthogonal planes for $n_x = 0$, $n_y = 0$, and $n_z = 0$. If the polynomial degree is only present in a single receive channel, a colored pixel value (x channel: red, y channel: green, z channel: blue) is rendered. If the polynomial degree is selected in multiple channels, the pixel is rendered in black. It can be seen that low polynomial degrees occur in at least two of three receive channels indicating a high redundancy across the receive channels. However, higher polynomial degrees between $n = 10$–14 are only selected in a single receive channel since the SNR in the other two channels is too low. In turn, these rows in the corresponding system matrices carry non-redundant information.

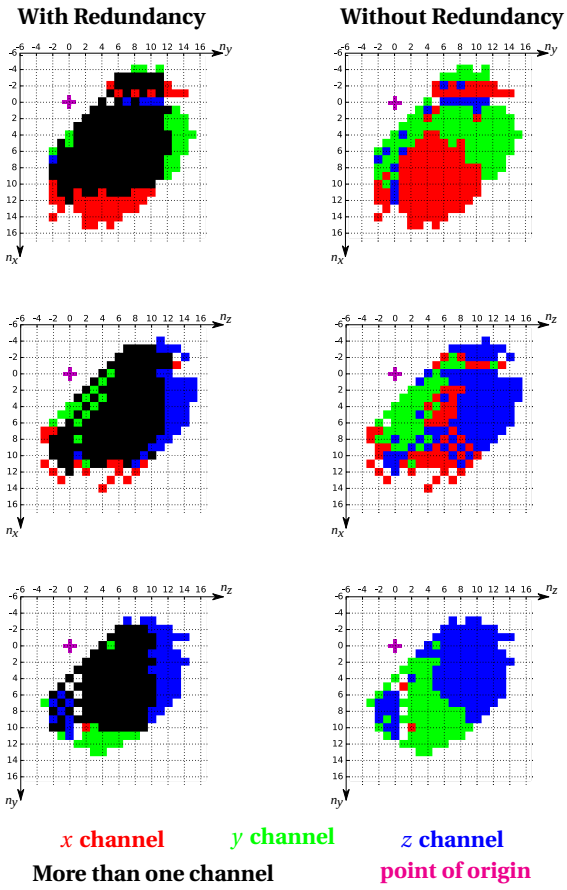

Figure 3: Graphical illustration of the frequency selection for different receive channels. Shown is a color coded mask encoding if the channel is selected in the x channel (red), the y channel (green), or the z channel (blue). The data is plotted against the polynomial degrees n_x, n_y, and n_z. If the corresponding degree is selected in multiple channels the pixel is rendered in black. Shown are the three main planes of the 3D frequency selection mask. On the left, the results without removal of redundant matrix rows are show. On the right, the frequency selection with redundancy removal are rendered.

Data Redundancy Reduction

Based on the data redundancy analysis we can introduce an additional frequency selection approach that removes all redundant matrix rows prior to reconstruction. To this end for each combination of mixing factors the SNR of the patterns in all three receive channels is compared and only the pattern with the highest SNR is selected for reconstruction.

Comparison of Selected Frequencies

The full system matrices $\boldsymbol{S}_l$, $l = x, y, z$ have each a total number of 26929 rows. Tab. 1 gives the number of matrix rows that are taken into account when applying an SNR threshold of 2.5. The results are reported for any combination of one, two, and three receive channels. Furthermore the number of selected matrix rows is given for the three channel reconstruction where additionally the redundant matrix rows of different receive channels have been removed.

A graphical illustration of the redundancy removal is given in Fig. 3. One can see that the redundant black pixels are fully removed and that one can directly see from which channel the corresponding polynomial degree is selected. One can clearly see that a diagonal structure is present such that in most cases that channel is selected in which the polynomial degree is maximum.

Table 1: Number of selected matrix rows used for reconstruction after applying an SNR threshold.

	x freq.	y freq.	z freq.	sum
***xyz* reconstruction**	**2318**	**2060**	**2150**	**6528**
x reconstruction	2318	-	-	2318
y reconstruction	-	2060	-	2060
z reconstruction	-	-	2150	2150
xy reconstruction	2318	2060	-	4378
yz reconstruction	-	2060	2150	4210
xz reconstruction	2318	-	2150	4468
reduced xyz reconst.	1190	971	1004	3165

II.III. Image Reconstruction

Image reconstruction is performed by solving the least squares problem

$$\underset{\boldsymbol{c}}{\operatorname{argmin}} \|\boldsymbol{S}\boldsymbol{c} - \boldsymbol{u}\|_2^2, \tag{10}$$

where different numbers of receive channels can be encoded in $\boldsymbol{S}$ and $\boldsymbol{u}$. The least squares problem is solved using the iterative Kaczmarz algorithm as discussed in [9, 14, 15]. The entire reconstruction framework is implemented using the scientific programming language Julia [16]. In contrast to former work outlined in [9] we apply

no explicit Tikhonov regularization to avoid smoothing the solution $\boldsymbol{c}$. We observed that it is possible to omit explicit Tikhonov regularization when applying an appropriate SNR threshold and using a fixed number of Kaczmarz iterations. Within this work a fixed number of 10 Kaczmarz iterations is chosen. Using the same set of reconstruction parameters ensures that the results for different numbers of receive channels can be directly compared. The reconstruction time using all 6528 matrix rows is about 7.5 s and linearly depends on the number of selected matrix rows.

III. Results

In Fig. 4 reconstruction results and profiles through the dot sample are shown. The first, second, and third row show the results using one, two, and all three receive channels, respectively. In the last row additionally the reconstruction using the reduced frequency selection is visualized.

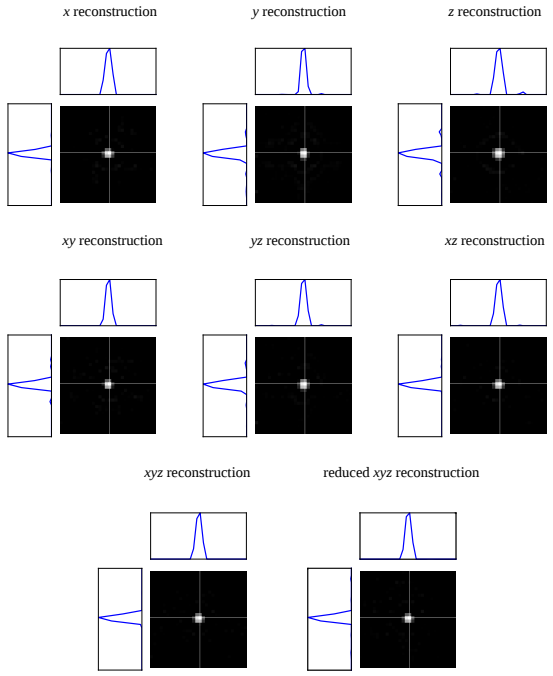

Figure 4: Reconstruction results and corresponding profiles through the delta sample. The first and the second row show the results using one and a combination of two receive channels, respectively. In the third row the reconstruction results using all selected frequencies (left) and with the removal of redundant frequencies (right) using all three receive channels are shown.

From a first sight it can be observed that all reconstruction results look very similar. No major degradation in image quality can be observed when reducing the number of receive channels. In order to compare the images quantitatively we calculate the FWHM of the point in all three directions, which is given in Tab. 2. Here, we use the reconstructed image obtained when selecting all three receive channels as the base reference. If one accounts for the doubled resolution in z direction due to the doubled gradient strength, the result is rather isotropic and does not favor a certain direction. Only in y direction, the resolution of 4.8 mm is slightly lower than in x direction.

Table 2: FWHM in mm through the dot sample reconstructed with different receive channel numbers and frequency selections. The reference reconstruction using all three receive channels is marked in bold. In brackets the deviation from to the reference reconstruction is reported.

	x profile	y profile	z profile
***xyz* reconst.**	**4.4**	**4.8**	**2.2**
x reconst.	4.4 (0%)	5.4 (+12%)	2.5 (+13%)
y reconst.	5.2 (+18%)	4.2 (-12%)	2.6 (+18%)
z reconst.	5.4 (+22%)	5.6 (+16%)	2.0 (-9%)
xy reconst.	4.4 (0%)	4.4 (-8%)	2.5 (+13%)
yz reconst.	5.2 (+18%)	4.8 (0%)	2.2 (0%)
xz reconst.	4.6 (+4%)	5.2 (+8%)	2.2 (0%)
reduced xyz reconst.	4.4 (0%)	4.8 (0%)	2.2 (0%)

When using a single receive channel one can directly see that the resolution gets anisotropic. In direction of the receive channel, the resolution is comparable to that of the three-channel reconstruction or even slightly better. In both other directions a loss in resolution of about 12 % to 22 % can be observed. When using two of three receive channels one observes an isotropic resolution in the plane spanned by both receive coils and a slightly degraded resolution along the axis, where the receive channel has been dropped.

When reducing the redundant frequency components of the three channel system matrix using the selection method outlined in Sec. II.II, it is possible to achieve nearly the same results as when taking all the redundant frequency components of all three receive channels into account. The resolution in terms of the FWHM remains unchanged.

We will next consider the reconstruction results from the five-point resolution phantom to confirm the results obtained by the dot phantom FWHM analysis. The reconstruction results and the corresponding profiles in x and y directions are shown in Fig. 5. One can see that the three dots in both direction can not be all resolved when using only one or two channels for reconstruction. In contrast, when using all three receive channels, it is clearly possible to resolve the three dots in both directions. When removing redundant matrix rows the quality of the three channel reconstruction remains unchanged. We note that for the five-point resolution phantom it may happen that partial volume effects occur since the

individual dots of the resolution phantom may not be positioned exactly on the grid used for system matrix acquisition.

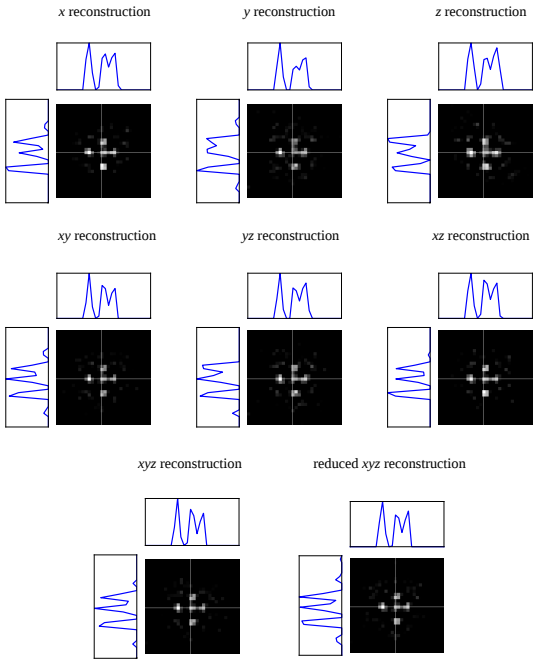

Figure 5: Reconstruction results and corresponding profiles through the five-point resolution phantom. The first and the second row show the results using one and a combination of two receive channels, respectively. In the third row the reconstruction results using all selected frequencies (left) and with the removal of redundant frequencies (right) using all three receive channels are shown.

IV. Discussion and Conclusion

In this work the influence of the receive channel selection on the image quality and the spatial resolution has been analyzed. The effects were studied using experimental data obtained using a delta sample and a resolution phantom.

Our study shows that in principle 3D Lissajous type MPI data can be reconstructed with only a single receive channel. A slight loss of spatial resolution in the order of 12 % to 22 % could be observed. Interestingly, the single-channel reconstruction partly even had a better resolution in terms of the FWHM in the direction of the receive channel. It is not fully clear what caused this improvement.

The experiments were explained by analyzing the MPI system matrix for different receive channel numbers. It was discussed that the same spatial pattern can be found in all three receive channels of the MPI system matrix. Since the signal level in the patterns corresponding to the same oscillating degree were significantly different, we observed that certain patterns were only available in one or two receive channels. This shows that taking all three receive channels into account during reconstruction does indeed give more linear independent information that can improve the image quality. However, at the same time we have shown that one can remove more than half of the redundant matrix rows across the receive channels without degradation of the resulting spatial resolution after reconstruction. This allows for reducing the reconstruction time in MPI, which is important for the realization of online reconstruction frameworks [17].

The findings of the present work can be used when designing future receive chains for 3D Lissajous type MPI scanners. For instance it could be advantages to only build a single channel receive coil that is tailored to maximize SNR by using all available space that is provided for the receiving unit instead of using three channels with reduced sensitivity. Furthermore, a single-channel receive setup is also easier to realize since 2D and 3D receive coil setups have to be manually decoupled. This could lower the effort to realize future MPI scanners.

Acknowledgment

The authors thankfully acknowledge the financial support by the German Research Foundation (DFG, grant numbers KN 1108/2-1 and AD 125/5-1).

References

[1] J. Franke, U. Heinen, H. Lehr, A. Weber, F. Jaspard, W. Ruhm, M. Heidenreich, and V. Schulz. System Characterization of a Highly Integrated Preclinical Hybrid MPI-MRI Scanner. *IEEE Trans. Med. Imag.*, 35(9):1993–2004, 2016. doi:10.1109/TMI.2016.2542041.

[2] B. Gleich and J. Weizenecker. Tomographic imaging using the nonlinear response of magnetic particles. *Nature*, 435(7046):1214–1217, 2005. doi:10.1038/nature03808.

[3] P. W. Goodwill and S. M. Conolly. The x-Space Formulation of the Magnetic Particle Imaging process: One-Dimensional Signal, Resolution, Bandwidth, SNR, SAR, and Magnetostimulation. *IEEE Trans. Med. Imag.*, 29(11):1851–1859, 2010. doi:10.1109/TMI.2010.2052284.

[4] P. W. Goodwill, G. C. Scott, P. P. Stang, and S. M. Conolly. Narrowband Magnetic Particle Imaging. *IEEE Trans. Med. Imag.*, 28(8):1231–1237, 2009. doi:10.1109/TMI.2009.2013849.

[5] T. Knopp, T. F. Sattel, and T. M. Buzug. Efficient Magnetic Gradient Field Generation With Arbitrary Axial Displacement for Magnetic Particle Imaging. *IEEE Magn. Lett.*, 3:6500104, 2012. doi:10.1109/LMAG.2011.2181341.

[6] T. F. Sattel, T. Knopp, S. Biederer, B. Gleich, J. Weizenecker, J. Borgert, and T. M. Buzug. Single-sided device for magnetic particle imaging. *J. Phys. D: Appl. Phys.*, 42(1):1–5, 2009. doi:10.1088/0022-3727/42/2/022001.

[7] P. Vogel, M. A. Rückert, P. Klauer, W. H. Kullmann, P. M. Jakob, and V. C. Behr. Traveling Wave Magnetic Particle Imaging. *IEEE Trans. Med. Imag.*, 33(2):400–407, 2014. doi:10.1109/TMI.2013.2285472.

[8] P. W. Goodwill, J. J. Konkle, B. Zheng, E. U. Saritas, and S. M. Conolly. Projection X-Space Magnetic Particle

Imaging. *IEEE Trans. Med. Imag.*, 31(5):1076–1085, 2012. doi:10.1109/TMI.2012.2185247.

[9] T. Knopp, M. Erbe, S. Biederer, T. F. Sattel, and T. M. Buzug. Efficient generation of a magnetic field-free line. *Med. Phys.*, 37(7): 3538–3540, 2010. doi:10.1118/1.3447726.

[10] T. Knopp, S. Biederer, T. Sattel, J. Weizenecker, B. Gleich, J. Borgert, and T. M. Buzug. Trajectory analysis for magnetic particle imaging. *Phys. Med. Biol.*, 54(2):385–397, 2009. doi:10.1088/0031-9155/54/2/014.

[11] J. Weizenecker, B. Gleich, J. Rahmer, H. Dahnke, and J. Borgert. Three-dimensional real-time in vivo magnetic particle imaging. *Phys. Med. Biol.*, 54(5):L1–L10, 2009.

[12] J. Rahmer, J. Weizenecker, B. Gleich, and J. Borgert. Analysis of a 3-D System Function Measured for Magnetic Particle Imaging. *IEEE Trans. Med. Imag.*, 31(6):1289–1299, 2012. doi:10.1109/TMI.2012.2188639.

[13] T. Knopp, J. Rahmer, T. F. Sattel, S. Biederer, J. Weizenecker, B. Gleich, J. Borgert, and T. M. Buzug. Weighted iterative reconstruction for magnetic particle imaging. *Phys. Med. Biol.*, 55(6):1577–1589, 2010. doi:10.1088/0031-9155/55/6/003.

[14] A. Dax. On row relaxation methods for large constrained least squares problems. *SIAM J. Sci. Comput.*, 14(3):570–584, 1993. doi:10.1137/0914036.

[15] S. Kaczmarz. Angenäherte Auflösung von Systemen linearer Gleichungen. *Bulletin of the International Academy Polonica Sciences Letters A*, 35:355 – 357, 1937.

[16] J. Bezanson, S. Karpinski, V. B. Shah, and A. Edelman. Julia: A Fast Dynamic Language for Technical Computing. *arXiv:1209.5145*, 2012. URL http://arxiv.org/abs/1209.5145.

[17] T. Knopp and M. Hofmann. Online reconstruction of 3D magnetic particle imaging data. *Phys. Med. Biol.*, 61(11):N257–N267, 2016. doi:10.1088/0031-9155/61/11/N257.

